Journal of Turbulence
Volume 6, No. 11, 2005

Taylor & Francis
Taylor & Francis Group

Coherent vortex extraction in 3D homogeneous turbulence: comparison between orthogonal and biorthogonal wavelet decompositions

O. ROUSSEL,†‡ K. SCHNEIDER,*§ and M. FARGE†

†Laboratoire de Météorologie Dynamique, Ecole Normale Supérieure, 24 rue Lhomond, 75231 Paris cedex 05, France
‡Institut für Technische Chemie und Polymerchemie, Universität Karlsruhe (TH), Kaiserstr. 12, 76128 Karlsruhe, Germany
§Laboratoire de Modélisation et Simulation Numérique en Mécanique, CNRS et Universités d'Aix-Marseille & CMI, Université de Provence, 39 rue Frédéric Joliot-Curie, 13453 Marseille cedex 13, France

A comparison between two different ways of extracting coherent vortices in three-dimensional (3D) homogeneous isotropic turbulence is performed, using either orthogonal or biorthogonal wavelets. The method is based on a wavelet decomposition of the vorticity field and a subsequent thresholding of the wavelet coefficients. The coherent vorticity is reconstructed from a few strong wavelet coefficients, while the incoherent vorticity is reconstructed from the remaining weak coefficients. The choice of the threshold, which has no adjustable parameters, is motivated for the orthogonal case from the denoising theory. Using only 3% of the coefficients we show that both decompositions, that is orthogonal and biorthogonal, extract the coherent vortices. They contain most of the energy (around 99% in both cases) and retain 74% and 68% of the enstrophy in the orthogonal and biorthogonal cases, respectively. The incoherent background flow for the orthogonal decomposition, which corresponds to 97% of the wavelet coefficients, is structureless, decorrelated, and has a Gaussian velocity probability distribution function (PDF). In contrast, for the biorthogonal decomposition, the background flow exhibits quasi-two-dimensional (2D) structures and yields an exponential velocity PDF. Moreover, the biorthogonal decomposition loses 3.7% of both enstrophy and helicity, while they are conserved by the orthogonal decomposition.

Keywords: Computational fluid mechanics; Coherent vortex simulation; Wavelets; Turbulence

1. Introduction

Many turbulent flows exhibit organized structures evolving in a random background. A separation of the flow into these two components is a prerequisite for a sound physical modelling of turbulence. Since these organized structures are well localized and excited on a wide range of scales, we have proposed to use the wavelet representation of the vorticity field to analyse [1], to extract [2–4], and to compute them [4, 5]. In [6] we have introduced the vortex extraction technique for two-dimensional (2D) flows using scalar-valued wavelet decompositions. In [2] we have extended this technique to three-dimensional (3D) flows using a vector-valued wavelet decomposition. Wavelet bases are well suited for this task, because they are made

*Corresponding author.

Journal of Turbulence
ISSN: 1468-5248 (online only)
http://www.tandf.co.uk/journals
DOI: 10.1080/14685240500149831

of self-similar functions well localized in both physical and spectral spaces [1] leading to an efficient hierarchical representation of intermittent data, such as turbulent flow fields.

Our motivation is to extract and characterize coherent structures assuming that the remaining diffusion transport corresponds to a Gaussian white noise, whose effect will be easy to model. Therefore, our main focus is not on the coherent structures themselves, but on the noise: coherent structures are, by definition, what remains after the denoising, while the noise is supposed to be Gaussian and decorrelated.

The vortex extraction method is based on a wavelet decomposition of the vorticity field, a subsequent thresholding of the wavelet coefficients, and a reconstruction from those coefficients whose modulus is above a given threshold. The threshold value is based on mathematical theorems yielding an optimal min–max estimator for denoising of intermittent data [7, 8] and it depends on the flow, enstrophy and the Reynolds number only. In [6] and [2] we showed for 2D and 3D turbulence, respectively, that few strong wavelet coefficients represent the organized part of the flow that is the coherent vortices. The remaining many weak wavelet coefficients represent the incoherent background flow, which is structureless and the effect of which on the coherent vortices may be modelled statistically.

Constructions composed of biorthogonal wavelets are more flexible and thus easier to use for solving partial differential equations (PDEs). In [9] first results of vortex extractions, later extended in [10], using lifted interpolating biorthogonal wavelets have been presented and compared with Daubechies orthogonal wavelets. It has been shown that these biorthogonal wavelets make it possible to get a higher optimal compression ratio than with the orthogonal wavelets. The discarded coefficients of the flow field, however, contain more coherent structures, and the optimal wavelet compression did not coincide with the theoretical compression predicted by Donoho [7]. An explanation given by the present authors is that the discarded part of the flow field does not correspond to Gaussian white noise [9].

The aim of the present paper is to assess the properties of the biorthogonal wavelet decomposition for coherent vortex extraction and to compare the results with those obtained using orthogonal wavelets. In [11] we have developed an adaptive multi-resolution method based on Harten's biorthogonal decomposition to solve nonlinear parabolic PDEs and have shown its computational efficiency. The extension of this scheme to the Navier–Stokes equations is currently under way. In the coherent vortex simulation (CVS) approach [5], the coherent flow is computed in an adaptive wavelet basis while the effect of the incoherent background flow is statistically modelled or just discarded. Hence, if the biorthogonal decomposition would yield similar filtering results for turbulent flows as the orthogonal decomposition, it would be advantageous to use biorthogonal wavelets to increase the performance of CVS. A crucial question, however, is to check if the incoherent part is statistically well behaved in order to be easier to model or even to be eliminated if it does not play any dynamic role.

The paper is organized as follows: in section 2 we recall the coherent vortex extraction algorithm and discuss its extension to biorthogonal wavelets using Harten's discrete multi-re-solution technique. Section 3 deals with the application of orthogonal and biorthogonal decompositions to direct numerical simulation (DNS) data of homogeneous isotropic turbulence. In section 4 we discuss the helicity and the Lamb vector of the two flow components for the different decompositions. Finally, conclusions are given in section 5 and we present some perspectives for turbulence modelling.

2. Coherent vortex extraction

In [2, 6] a wavelet-based method to extract coherent vortices out of both 2D and 3D turbulent flows was proposed. The principle is to split a turbulent flow into a coherent and an incoherent

part. For this we use a 3D vector-valued multi-resolution analysis (MRA) of $(L^2(\mathbb{R}^3))^3$, that is a set of nested subspaces $\vec{V}_j \subset \vec{V}_{j+1}$ for $j = 0, \ldots, J-1$, representing the flow at different scales $l = 2^{-j}$. Considering the complement spaces $\vec{W}_j = \vec{V}_{j+1} \ominus \vec{V}_j$, we obtain a wavelet representation.

Let us consider a 3D vorticity field $\vec{\omega}(\vec{x}) = \vec{\nabla} \times \vec{v}(\vec{x})$, and its projection $P_J\vec{\omega} = \vec{\omega}^J$ on a grid at resolution $N = 2^{3J}$, where N is the number of grid points and J denotes the number of scales in each direction. The projected vorticity field can be expressed in a wavelet series using a 3D MRA

$$\vec{\omega}^J(\vec{x}) = \vec{\bar{\omega}}_{0,0,0}\ \Phi_{0,0,0}(\vec{x}) + \sum_{j=0}^{J-1} \sum_{i_x,i_y,i_z=1}^{2^j-1} \sum_{\mu=1}^{7} \vec{\tilde{\omega}}^{\mu}_{j,i_x,i_y,i_z} \Psi^{\mu}_{j,i_x,i_y,i_z}(\vec{x}) \tag{1}$$

where Φ_{i_x,i_y,i_z} denotes the 3D scaling function, defined as

$$\Phi_{j,i_x,i_y,i_z}(\vec{x}) = \phi_{j,i_x}(x)\ \phi_{j,i_y}(y)\ \phi_{j,i_z}(z)$$

and Ψ_{j,i_x,i_y,i_z} denotes the corresponding 3D wavelet, that is

$$\Psi^{\mu}_{j,i_x,i_y,i_z} = \begin{cases} \psi_{j,i_x}(x)\ \phi_{j,i_y}(y)\ \phi_{j,i_z}(z) & \text{if} \quad \mu = 1 \\ \phi_{j,i_x}(x)\ \psi_{j,i_y}(y)\ \phi_{j,i_z}(z) & \text{if} \quad \mu = 2 \\ \phi_{j,i_x}(x)\ \phi_{j,i_y}(y)\ \psi_{j,i_z}(z) & \text{if} \quad \mu = 3 \\ \psi_{j,i_x}(x)\ \phi_{j,i_y}(y)\ \psi_{j,i_z}(z) & \text{if} \quad \mu = 4 \\ \psi_{j,i_x}(x)\ \psi_{j,i_y}(y)\ \phi_{j,i_z}(z) & \text{if} \quad \mu = 5 \\ \phi_{j,i_x}(x)\ \psi_{j,i_y}(y)\ \psi_{j,i_z}(z) & \text{if} \quad \mu = 6 \\ \psi_{j,i_x}(x)\ \psi_{j,i_y}(y)\ \psi_{j,i_z}(z) & \text{if} \quad \mu = 7 \end{cases}$$

Here ϕ_{j,i_x} denotes the one-dimensional (1D) scaling function, ψ_{j,i_x} the corresponding (1D) wavelet, j the index for the scale, i_x, i_y, i_z the indices for the translation, and μ the index for the seven discrete directions in 3D.

For the orthogonal decomposition, we use Coifman 12 wavelets, which have four vanishing moments, because they are almost symmetric and compactly supported [2]. Note that we compared the results obtained for Coifman 12 wavelets with Coifman 6 wavelets (two vanishing moments) and found no significant difference. Owing to orthogonality, the scaling and wavelet coefficients are given by $\bar{\omega}_{0,0,0} = \langle \vec{\omega}, \Phi_{0,0,0} \rangle$ and $\tilde{\vec{\omega}}_{j,i_x,i_y,i_z} = \langle \vec{\omega}, \Psi_{j,i_x,i_y,i_z} \rangle$, where $\langle \cdot, \cdot \rangle$ denotes the L^2-inner product. The 1D scaling function and wavelet are plotted in figure 1.

For the biorthogonal decomposition, we have chosen the scaling function and the wavelet corresponding to Harten's multi-resolution [12]. In this case, projection and prediction

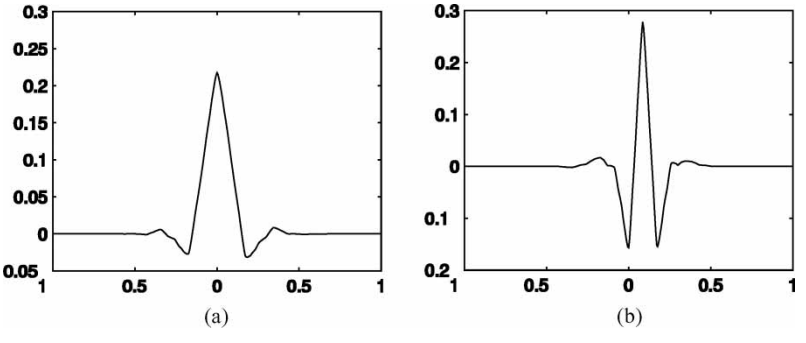

Figure 1. Orthogonal wavelet (Coifman 12): (a) scaling function ϕ and (b) wavelet ψ.

operators are defined to map the solution on a set of dyadic grids covering the domain [11]. The approximation of physical quantities on the grid is no longer expressed as point values, but as cell averages. The projection operator, which maps the cell averages on the finer grid onto those of the coarser grid, is exact and unique, since the cell averages on the coarser grid are nothing but the averages of the cell averages on the next finer grid. The prediction operator, which maps the solution on the finer grid from the solution on a coarser grid, uses a polynomial interpolation from the nearest neighbours. Here we choose to use only the nearest neighbour in each direction, diagonal included, which corresponds to a third-order polynomial interpolation. In the following, the wavelet corresponding to the prediction operator based on the third-order polynomial interpolation is called Harten 3 wavelet, which has three vanishing moments [13]. Since the wavelet basis is biorthogonal, the scaling and wavelet coefficients are $\vec{\tilde{\omega}}_{0,0,0} = \langle \vec{\omega}, \Phi^{\star}_{0,0,0} \rangle$ and $\vec{\tilde{\omega}}_{j,i_x,i_y,i_z} = \langle \vec{\omega}, \Psi^{\star}_{j,i_x,i_y,i_z} \rangle$, where $\Phi^{\star}$ and $\Psi^{\star}$ respectively denote the dual scaling function and the dual wavelet [13]. The 1D scaling function, the wavelet, and the corresponding duals are plotted in figure 2.

The vortex extraction algorithm can be summarized as follows:

(1) given $\vec{\omega}(\vec{x})$, sampled on a grid $(x_{i_x}, y_{i_y}, z_{i_z})$ for $i_x, i_y, i_z = 0, \ldots, 2^J - 1$, and the total enstrophy $Z = \frac{1}{2}\langle \vec{\omega}, \vec{\omega} \rangle$;
(2) perform the 3D wavelet decomposition (that is, apply the fast wavelet transform (FWT) [1] to each component of $\vec{\omega}$) to obtain $\vec{\tilde{\omega}}_{0,0,0}$ and $\vec{\tilde{\omega}}^{\mu}_{j,i_x,i_y,i_z}$ for $j = 0, \ldots, J-1$, $i_x, i_y, i_z = 0, \ldots, 2^{J-1} - 1$, and $\mu = 1, \ldots, 7$;

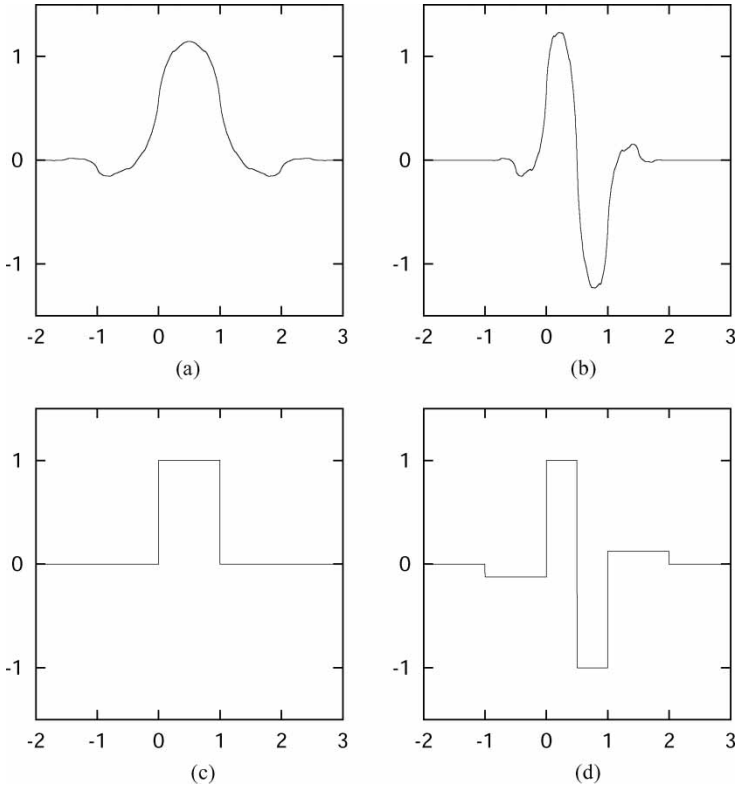

Figure 2. Biorthogonal wavelet (Harten 3): (a) scaling function ϕ, (b) wavelet ψ, (c) dual scaling function $\Phi^{\star}$, (d) and dual wavelet $\Psi^{\star}$.

(3) compute the threshold $\epsilon_T = (\frac{4}{3} Z \ln N)^{1/2}$ and threshold the coefficients $\tilde{\vec{\omega}}$ to obtain

$$\tilde{\vec{\omega}}_c = \begin{cases} \tilde{\vec{\omega}} & \text{for } |\tilde{\vec{\omega}}| > \epsilon_T \\ 0 & \text{else} \end{cases} \qquad \tilde{\vec{\omega}}_i = \begin{cases} \tilde{\vec{\omega}} & \text{for} |\tilde{\vec{\omega}}| \leq \epsilon_T \\ 0 & \text{else,} \end{cases} \tag{2}$$

the subscripts c and i denoting the coherent and incoherent parts;

(4) perform the 3D wavelet reconstruction (that is apply the inverse FWT [1]) to compute $\vec{\omega}_c$ and $\vec{\omega}_i$ from $\tilde{\vec{\omega}}_c$ and $\tilde{\vec{\omega}}_i$, respectively;

(5) use Biot–Savart's relation $\vec{v} = \nabla \times (\nabla^{-2} \vec{\omega})$ to reconstruct the coherent and incoherent velocity fields from the coherent and incoherent vorticity fields, respectively.

This decomposition yields $\vec{\omega} = \vec{\omega}_c + \vec{\omega}_i$ and $\vec{v} = \vec{v}_c + \vec{v}_i$. In the orthogonal case we have $\langle \vec{\omega}_c, \vec{\omega}_i \rangle = 0$ and hence it follows that $Z = Z_c + Z_i$. This enstrophy conservation is only approximately fulfilled in the biorthogonal case. As the Biot–Savart operator is not diagonal in wavelet space, we have for both decompositions $E = E_c + E_i + \varepsilon$, where $E = \frac{1}{2} \langle \vec{v}, \vec{v} \rangle$ and ε remains small (see Section 3).

Note that the coherent and incoherent vorticity fields are not perfectly solenoidal, as discussed in [3]. The coherent and incoherent velocity fields are, however, divergence-free, thanks to the Biot–Savart reconstruction, that is the divergent part has been removed. Furthermore, we have shown in [3] that the non-solenoidal contribution remains below 2.9% of the total coherent enstrophy and only appears in the dissipative range. The fact that there is no divergent contribution in the inertial range guarantees that the nonlinear dynamics, and therefore the flow evolution, are not affected by the divergent contribution of the vorticity. Several ways to ensure that the coherent and incoherent vorticities remain solenoidal are given in [3].

In the case of orthogonal wavelets the choice of the threshold ϵ_T is motived by the Donoho filtering procedure for signal denoising [7, 8]. The threshold $\epsilon_T = (\frac{4}{3} Z \ln N)^{1/2}$ depends on the total enstrophy Z and on the resolution N, that is it has no adjustable parameters. The coherent vorticity is reconstructed from those wavelet coefficients with modulus larger than the threshold, while the remaining part corresponds to an incoherent noise. This procedure has been successfully applied to extract coherent vortices out of isotropic homogeneous turbulent flows in [3] and out of turbulent mixing layers in [4].

Donoho and Johnstone [7, 8] considered the case of noisy data which consist of a signal plus an additive Gaussian white noise. Using the above procedure with threshold ϵ_T, where $2Z$ denotes the variance of the noise, they have shown that a signal can be recovered in an optimal way. As the threshold depends on the sampling size and on the variance of the noise, and not on the signal itself, it is sometimes called the universal threshold. Theorems prove that this technique yields a min–max estimator for denoising, which means that the maximum quadratic error between the denoised signal and the original signal is minimized for signals with inhomogenous regularity, like intermittent signals [7, 8].

In the present case we over estimate the variance of the noise by using the variance of the total flow instead. An algorithm for estimating the variance of the noise iteratively was proposed in [6] and mathematically justified in [14].

For the biorthogonal case, since no optimal threshold exists a priori, we have decided to retain the same number of coefficients as for the orthogonal case, in order to compare both representations for the same compression rate. Let us mention that the complexity of the FWT is in both cases of $O(N)$, where N denotes the total number of grid points. The reconstruction of the velocity field from the corresponding vorticity using the Biot–Savart relation is however, done in Fourier space using a fast Fourier transform (FFT). Hence the total complexity of the above algorithm becomes $O(N \log_2 N)$.

3. Comparison for vorticity and velocity

We apply the coherent vortex extraction algorithm to DNS data computed for a statistically stationary 3D homogeneous isotropic turbulent flow, forced at the largest scale, and whose turbulence level corresponds to a microscale Reynolds number $R_\lambda = 150$ [15]. This dimensionless number is defined as

$$R_\lambda = \frac{\lambda V_{\text{rms}}}{\nu}$$

where $\lambda = (E/Z)^{1/2}$ denotes the Taylor microscale, V_{rms} the root-mean-square velocity, and ν the kinematic viscosity.

The initial conditions are random and the boundary conditions are periodic. The flow was computed using a pseudo-spectral code at resolution 240^3 [15], upsampled to 256^3. Although this flow is statistically homogeneous and isotropic, vortex tubes are formed during the flow evolution (see figure 3).

The coherent vortex extraction algorithm is applied to the vorticity field shown in figure 3 using either Coifman 12 or Harten 3 wavelets. In figures 3 and 4, the modulus of the total, coherent, and incoherent vorticities resulting from the coherent vortex extraction are displayed for Coifman 12 and Harten 3 wavelet decompositions. In both cases, the isosurfaces, from light to dark, correspond to $||\vec{\omega}|| = 3\sigma$, 4σ, and 5σ for the total and coherent vorticities, and $||\vec{\omega}|| = \frac{3}{2}\sigma$, 2σ, and $\frac{5}{2}\sigma$ for the incoherent vorticity. Here $\sigma = \sqrt{2Z}$ denotes the variance of the vorticity fluctuations, Z being the total enstrophy.

By observing the coherent vorticity (figure 4(a) and (c)), we see that both decompositions, using either orthogonal or biorthogonal wavelets, retain the coherent vortices present in the total vorticity (figure 3). We find, however, that the incoherent vorticity is different for both decompositions: the incoherent vorticity obtained from the orthogonal decomposition (figure 4(b) and (d)) is structureless, whereas some coherent structures remain in the incoherent vorticity when one uses the biorthogonal decomposition.

The statistics of the resulting fields are given in table 1. We observe that, for both decompositions, only 3% wavelet modes retain about 99% of the total energy, while the remaining 97% modes contain less than 1% of the energy. Let us note that the loss of total energy for both decompositions (see explanation in section 2) remains small: 0.4% for the orthogonal case and

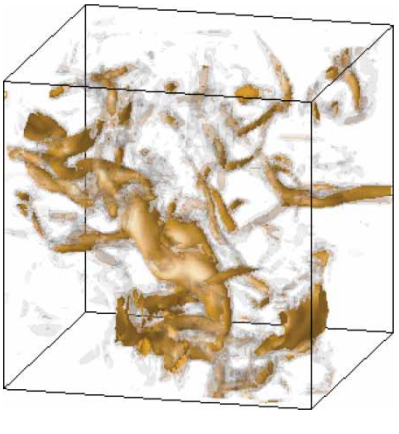

Figure 3. Modulus of the vorticity for the total field. Zoom of the top-left-front sub-cube of size 64^3. The surfaces, from light to dark, correspond to $||\vec{\omega}|| = 3\sigma$, 4σ, and 5σ, with $\sigma = \sqrt{2Z}$.

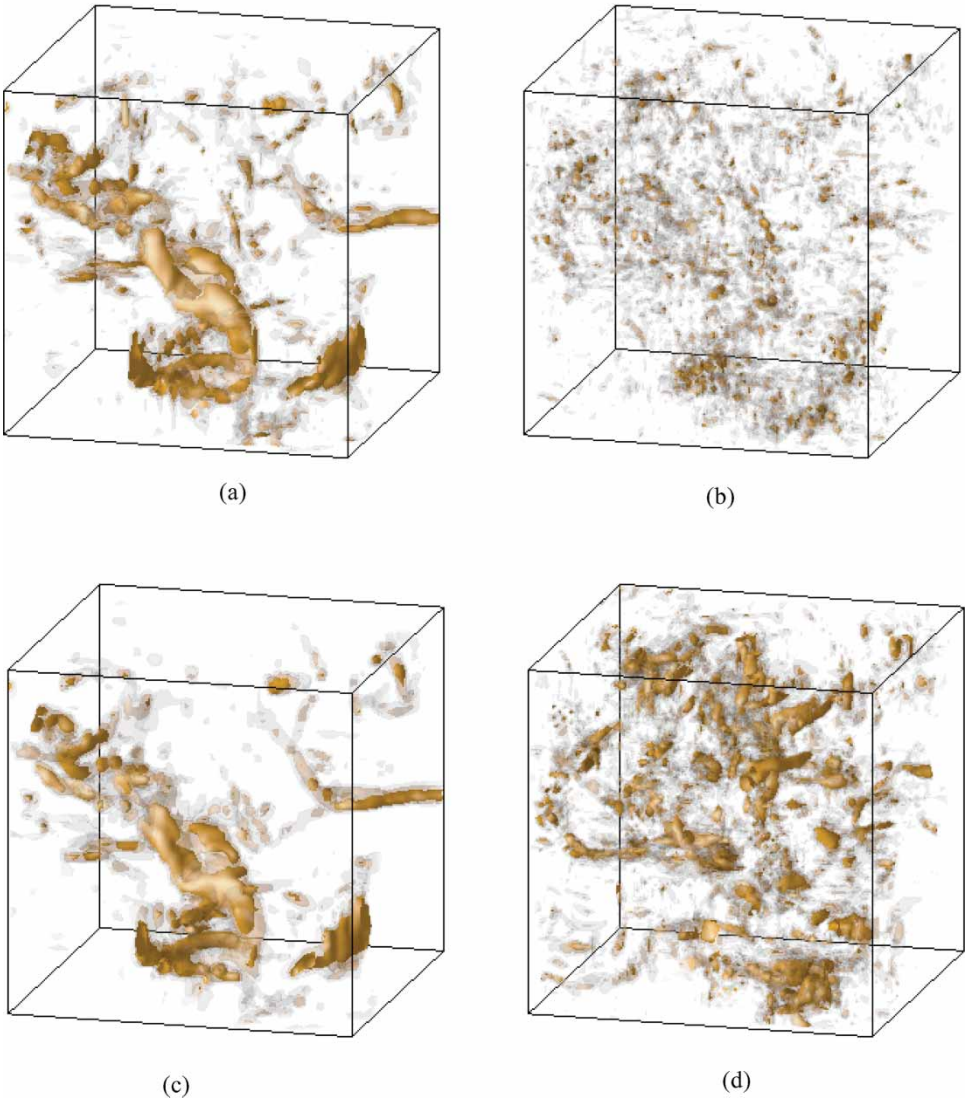

Figure 4. Comparison between orthogonal wavelet (a) and (b) and biorthogonal wavelet decompositions (c) and (d): Modulus of the vorticity for the retained (a) and (c) and discarded modes (b) and (d). Zoom of the top-left-front sub-cube of size 64^3. The surfaces, from light to dark, correspond to $||\vec{\omega}|| = 3\sigma$, 4σ, and 5σ on the left side, $||\vec{\omega}|| = \frac{3}{2}\sigma$, 2σ, and $\frac{5}{2}\sigma$ on the right side.

0.7% for the biorthogonal. We have shown [6] that for the orthogonal wavelet decomposition the energy lost only affects the dissipative scales, and can thus be neglected.

Concerning the enstrophy, we observe a significant difference between both methods: the 3% largest coefficients retain 75.5% of the total enstrophy with the orthogonal wavelets, whereas they retain only 69% for the biorthogonal wavelets. Moreover, 3.7% of the total enstrophy is lost in the biorthogonal decomposition, whereas it is fully conserved in the orthogonal decomposition.

Figure 5 shows the probability distribution function (PDF) of vorticity in semi-logarithmic coordinates. For both decompositions, the coherent vorticity shows a similar stretched

Table 1. Statistical properties of the vorticity and velocity fields for the orthogonal (Coifman 12) and biorthogonal (Harten 3) decompositions.

		Orthogonal		Biorthogonal	
Decomposition field	Total	Coherent	Incoherent	Coherent	Incoherent
% of coefficients	100.0%	3.0%	97.0%	3.0%	97.0%
Enstrophy	151.6	114.5	37.1	104.6	41.4
% of enstrophy	100.0%	75.5%	24.5%	69.0%	27.3%
Vorticity skewness	2.0×10^{-4}	-6.7×10^{-4}	-8.2×10^{-4}	-9.6×10^{-5}	-5.3×10^{-3}
Vorticity flatness	9.2	11.1	4.8	11.5	7.9
Energy	1.358	1.344	0.008	1.338	0.010
% of energy	100.0%	99.0%	0.6%	98.6%	0.7%
Velocity skewness	-1.1×10^{-1}	-1.1×10^{-1}	-9.2×10^{-4}	-1.1×10^{-1}	-3.4×10^{-4}
Velocity flatness	2.7	2.7	3.4	2.7	6.8

exponential behaviour as the total vorticity, with flatness 11.1 (Coifman 12) and 11.5 (Harten 3), compared with 9.2 for the total vorticity (table 1). Furthermore, the incoherent vorticity has an exponential PDF, but the flatness is about 1.6 times smaller in the orthogonal case than in the biorthogonal case (4.8 versus 7.9). Moreover, the extrema of the incoherent vorticity are about three times weaker than those of the coherent vorticity with the orthogonal wavelets, whereas this ratio is only about 2 for biorthogonal wavelets. Finally, the skewness of the total vorticity is about zero, and both extraction methods preserve this property (table 1).

Figure 6 shows the PDF of velocity in semi-logarithmic coordinates. First, we observe that both methods preserve the skewness of the total velocity, as was the case for the vorticity. We also note that the coherent velocity has the same Gaussian distribution as the total velocity, with flatness 2.7, whatever the decomposition. For the orthogonal decomposition, however, the PDF of the incoherent velocity is also almost Gaussian, with flatness 3.4, whereas it is exponential, with flatness 6.8, for the biorthogonal decomposition.

Figure 7 shows the 1D isotropic energy spectrum

$$E(k) = \sum_{k-\frac{1}{2}<k=|\vec{k}|\leq k+\frac{1}{2}} |\widehat{\vec{v}}(\vec{k})|^2$$

for the total, coherent and incoherent flows for both orthogonal and biorthogonal decompositions. The above equation denotes the Fourier transform. In both cases, we observe that the

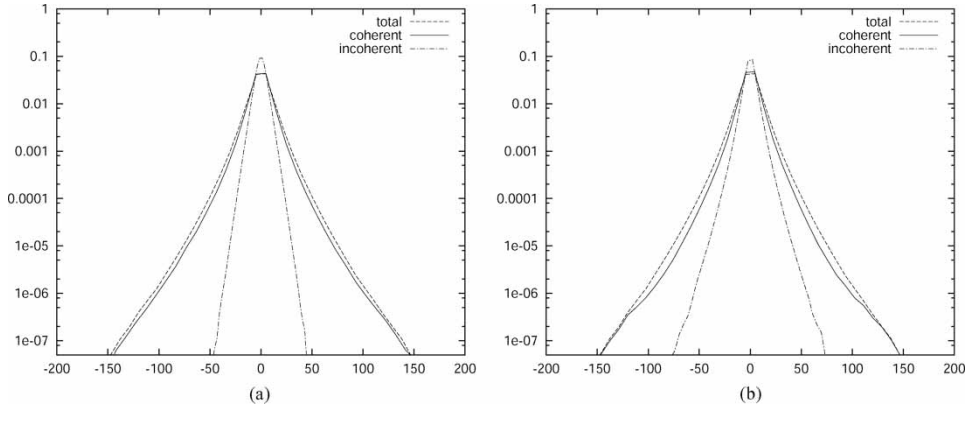

Figure 5. Comparison between orthogonal (a) and biorthogonal (b) wavelet decompositions: PDF of vorticity.

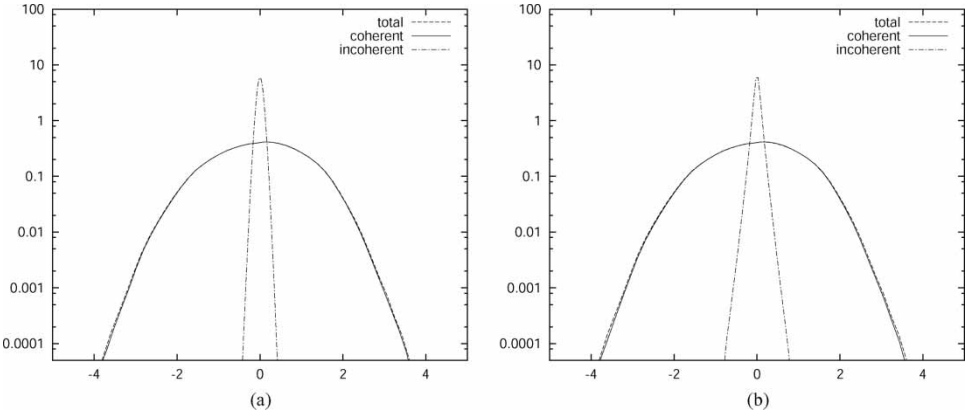

Figure 6. Comparison between orthogonal (a) and biorthogonal (b) wavelet decompositions: PDF of velocity.

energy spectrum of the coherent flow is identical to that of the total flow all along the inertial range, whereas it differs for $k \geq 30$, which is in the dissipative range. For the incoherent flow, we observe that $E(k)$ is close to k^2, which corresponds to an equipartition of energy, that is the velocity is decorrelated in physical space.

4. Comparison for helicity and Lamb vector

Coherent structures encountered in turbulent flows correspond to regions where the nonlinearity of Navier–Stokes equations is depleted [2, 6, 16]. For 2D incompressible flows this leads to a theoretical prediction stating that vorticity and stream function are related by a monotonous function, called the coherence function. In [6] we used wavelets to extract coherent vortices out of a 2D turbulent flow and checked a posteriori that our algorithm was successful by comparing the coherence function for the total, coherent, and incoherent flows. Such a simple criterion as the coherence function cannot be used for 3D flows since the stream function can no longer be uniquely defined in this case. In [2] we proposed to consider the local Beltramization of the flow to characterize coherent vortices that correspond to regions

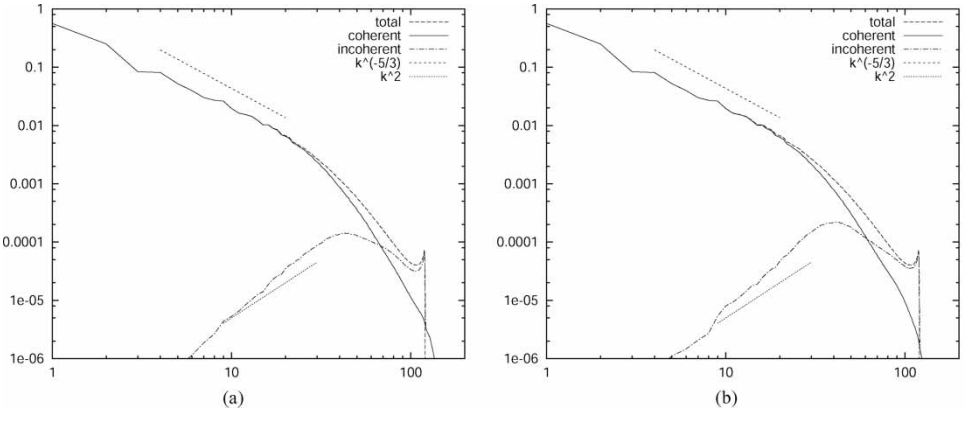

Figure 7. Comparison between orthogonal (a) and biorthogonal (b) wavelet decompositions: energy spectrum.

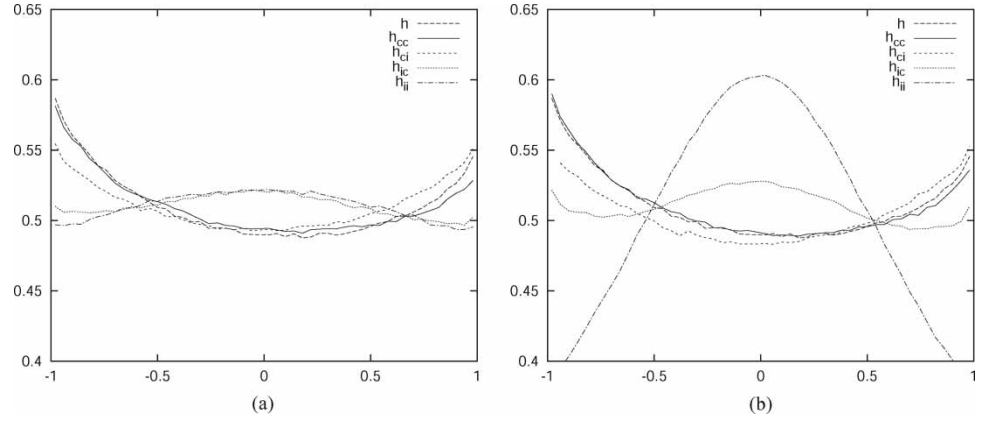

Figure 8. Comparison between orthogonal (a) and biorthogonal (b) wavelet decompositions: PDF of relative helicity.

in which the nonlinearity is depleted and which maximize the relative helicity, defined as

$$h(\vec{v},\vec{\omega}) = \frac{\vec{v}\cdot\vec{\omega}}{||\vec{v}||\ ||\vec{\omega}||}$$

One should notice that such a characterization corresponds to a special case of nonlinearity depletion and does not prove that we have extracted all coherent vortices, as is the case with the coherence function used to check our algorithm for 2D turbulent flows.

Figure 8 shows the PDF of the relative helicity for orthogonal and biorthogonal coherent vortex extractions. In both cases we split the relative helicity into four contributions: $h_{cc} = h(\vec{v}_c,\vec{\omega}_c)$, $h_{ci} = h(\vec{v}_c,\vec{\omega}_i)$, $h_{ic} = h(\vec{v}_i,\vec{\omega}_c)$, $h_{ii} = h(\vec{v}_i,\vec{\omega}_i)$. For both decompositions, we observe that the relative helicities based on the coherent velocity, that is h_{cc} and h_{ci}, exhibit the same PDF as those of the total flow, with two maxima at $h = \pm 1$, which correspond to helical vortex tubes for which velocity and vorticity vectors are parallel or antiparallel. In contrast, the PDF of the helicities based on the incoherent velocity, that is h_{ic} and h_{ii}, are maximal at $h = 0$, which suggests a tendency towards two-dimensionalization which appears more pronounced for the biorthogonal decomposition. These observations are consistent with the proposition of Keith Moffatt stating that '*blobs of maximal helicity may be interpreted as coherent structures, separated by regular surfaces on which vortex sheets, the site of strong dissipation, may be located* ' [16].

To try to obtain a better insight to characterize coherent vortices in 3D turbulent flows, let us consider Euler's equations written in Lamb's form

$$\frac{\partial\vec{\omega}}{\partial t} - \vec{\nabla}\times\vec{l} = \vec{0}$$
$$\vec{\nabla}\cdot\vec{v} = 0 \qquad (3)$$

where $\vec{l} = \vec{v}\times\vec{\omega}$ is the Lamb vector.

Since coherent vortices correspond to quasi-steady solutions [2], the nonlinear term $\vec{\nabla}\times\vec{l}$ should be zero. We thus propose to study the Lamb vector and its variance $\Lambda = \frac{1}{2}\langle\vec{l},\vec{l}\rangle$. As for the helicity, we split it into four contributions: $\vec{l}_{cc} = \vec{v}_c\times\vec{\omega}_c$ (coherent velocity × coherent vorticity), $\vec{l}_{ci} = \vec{v}_c\times\vec{\omega}_i$ (coherent velocity × incoherent vorticity), $\vec{l}_{ic} = \vec{v}_i\times\vec{\omega}_c$ (incoherent velocity × coherent vorticity) and $\vec{l}_{ii} = \vec{v}_i\times\vec{\omega}_i$ (incoherent velocity × incoherent vorticity).

Table 2. Analysis of the different contributions to the variance Λ of the Lamb vector $\vec{l}$ for the orthogonal (Coifman 12) and biorthogonal (Harten 3) wavelet decompositions.

	Orthogonal		Biorthogonal	
Decomposition	Value	%	Value	%
Λ	279.3	100.0	279.3	100.0
$\Lambda_{cc} = \frac{1}{2} < \vec{l}_{cc}, \vec{l}_{cc} >$	210.7	75.4	193.9	69.4
$\Lambda_{ci} = \frac{1}{2} < \vec{l}_{ci}, \vec{l}_{ci} >$	66.7	23.9	72.0	25.8
$\Lambda_{ic} = \frac{1}{2} < \vec{l}_{ic}, \vec{l}_{ic} >$	1.5	0.5	1.8	0.6
$\Lambda_{ii} = \frac{1}{2} < \vec{l}_{ii}, \vec{l}_{ii} >$	0.4	0.2	1.3	0.5
$\Delta = \Lambda - (\Lambda_{cc} + \Lambda_{ci} + \Lambda_{ic} + \Lambda_{ii})$	0.0	0.0	10.3	3.7

In table 2 we observe that for both orthogonal and biorthogonal decompositions, Λ_{cc} is the largest contribution, then Λ_{ci} is much weaker, while Λ_{ic} and Λ_{ii} are negligible. The coherent–coherent contribution Λ_{cc} is better retained by the orthogonal than by the biorthogonal wavelet decomposition. As a consequence, the incoherent contributions Λ_{ic} and Λ_{ii} are weaker for the orthogonal decomposition, which is also seen on the PDF of the Lamb vector (figure 9). Moreover, the biorthogonal decomposition is not conservative since 3.7% Λ is lost, which is not the case for the orthogonal decomposition.

Visualizations of isosurfaces of the Lamb vector are shown in figure 10 for the total field, in figure 11 for the coherent, and in figure 12 for the incoherent contributions using either the orthogonal or the biorthogonal wavelet decomposition. We first consider the coherent contributions $\vec{l}_{cc} = \vec{v}_c \times \vec{\omega}_c$ and $\vec{l}_{ci} = \vec{v}_c \times \vec{\omega}_i$. In figure 11 we observe that these coherent contributions present structures quite similar to the tube-like structures of the Lamb vector (figure 10) for both decompositions. We then consider the incoherent contributions $\vec{l}_{ic} = \vec{v}_i \times \vec{\omega}_c$ and $\vec{l}_{ii} = \vec{v}_i \times \vec{\omega}_i$. Notice that the isosurfaces for the incoherent contributions (figure 12) have been taken six times weaker than for coherent contributions (figure 11). We observe that only $\vec{l}_{ic}$ presents structures similar to those of the total Lamb vector (figure 10), and this is true for both decompositions. This is no longer the case for $\vec{l}_{ii}$, which is very weak and noise-like for the orthogonal wavelet decomposition (figure 12(b)), but not for the biorthogonal wavelet decomposition (figure 12(d)), because it is stronger and exhibits some organized structures. This is another reason, besides the enstrophy and helicity conservation property, to prefer the orthogonal decomposition.

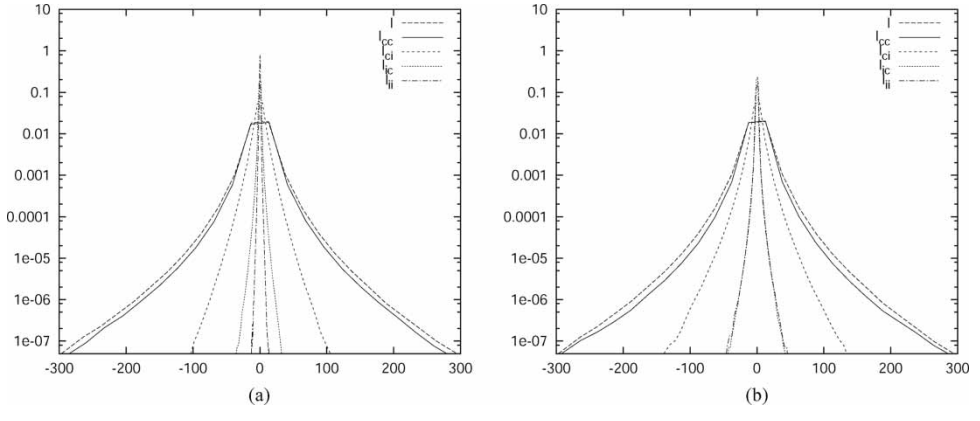

Figure 9. Comparison between orthogonal (a) and biorthogonal (b) wavelet decompositions: PDF of the Lamb vector.

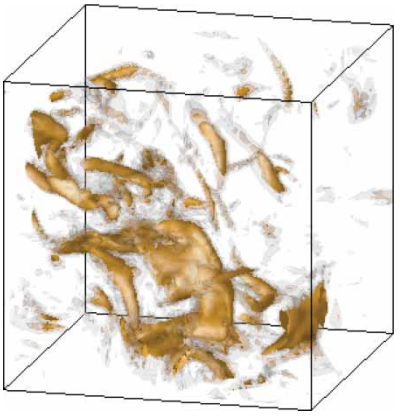

Figure 10. Modulus of the Lamb vector for the total field. Zoom of the top-left-front sub-cube of size 64^3. The surfaces, from light to dark, correspond to $||\vec{l}|| = 3\sigma'$, $4\sigma'$, and $5\sigma'$, with $\sigma' = \sqrt{2\Lambda}$.

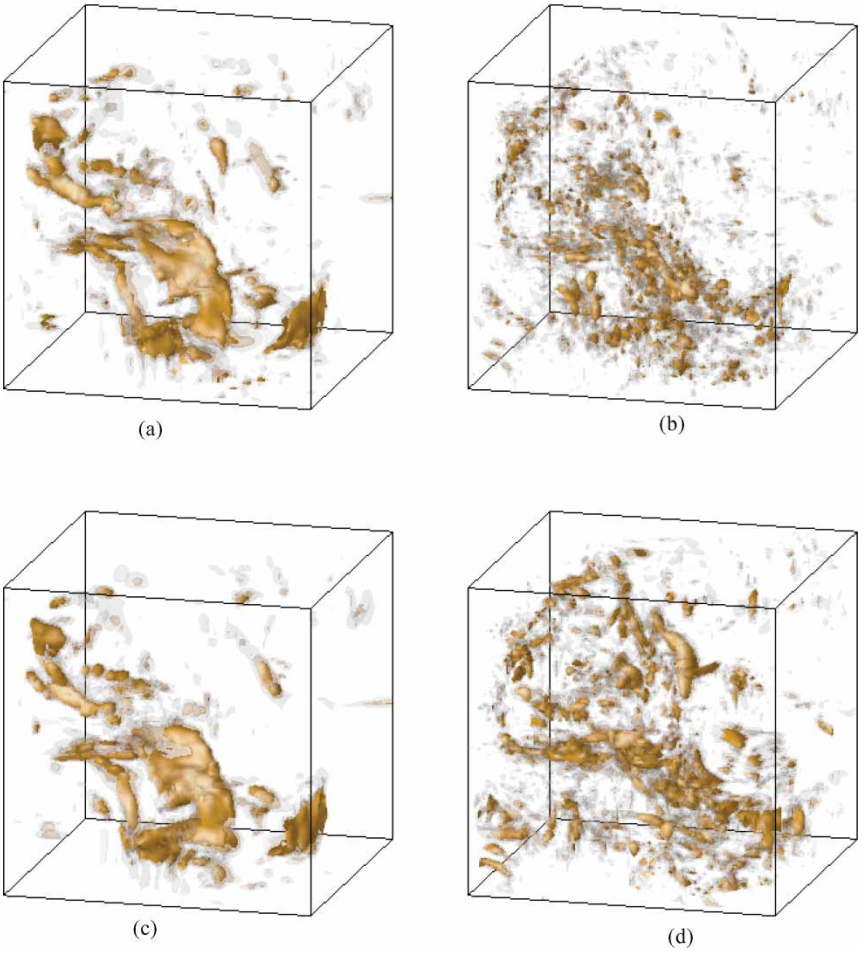

Figure 11. Comparison between orthogonal (a) and (b) and biorthogonal (c) and (d) wavelet decompositions: Modulus of $\vec{l}_{cc}$ (a) and (c) and $\vec{l}_{ci}$ (b) and (d). Zoom of the top–left–front sub-cube of size 64^3. The surfaces, from light to dark, correspond to $||\vec{l}|| = 3\sigma'$, $4\sigma'$, and $5\sigma'$ for the left pictures, $||\vec{l}|| = \frac{3}{2}\sigma'$, $\frac{4}{2}\sigma'$, and $\frac{5}{2}\sigma'$ for the right pictures.

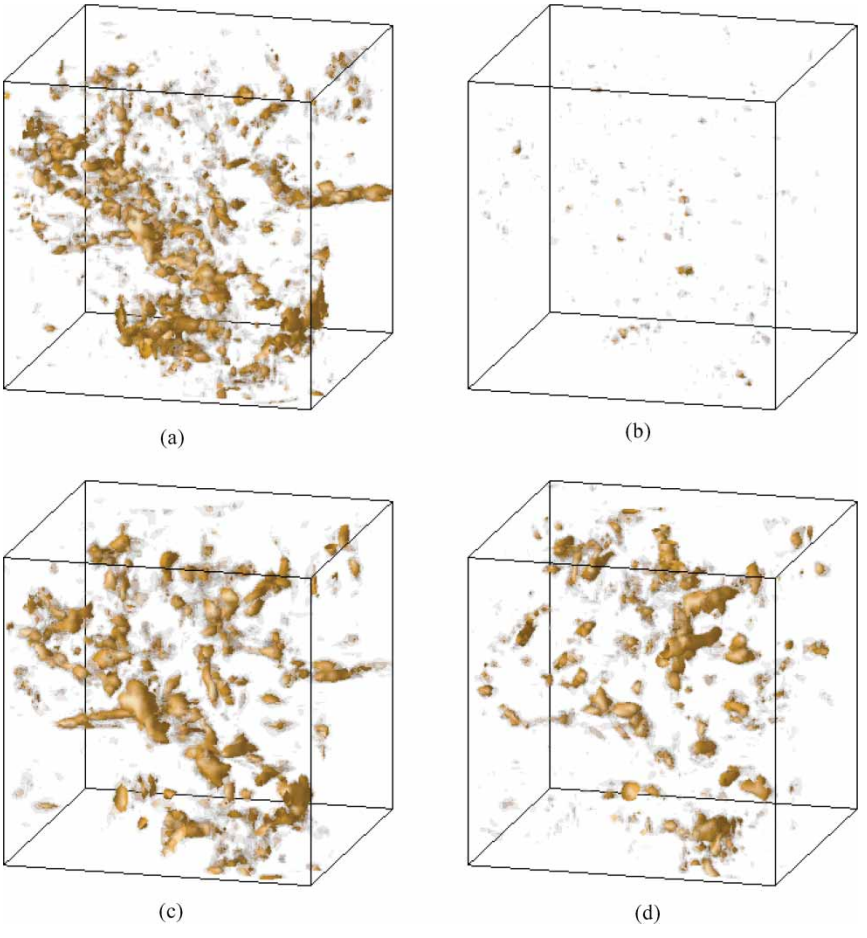

Figure 12. Comparison between Coifman 12 orthogonal (a) and (b) wavelet and Harten 3 biorthogonal (c) and (d) wavelet decompositions: Modulus of $\vec{l}_{ic}$ (a) and (c) and $\vec{l}_{ii}$ (b) and (d). Zoom of the top-left-front sub-cube of size 64^3. The surfaces, from light to dark, correspond to $||\vec{l}|| = \frac{3}{12}\sigma'$, $\frac{4}{12}\sigma'$, and $\frac{5}{12}\sigma'$.

5. Conclusions and perspectives

A homogeneous isotropic turbulent flow computed by DNS has been decomposed into a coherent and an incoherent flow, using either orthogonal or biorthogonal wavelet decompositions of the vorticity field. Both algorithms are of linear complexity, that is $O(N)$ where N denotes the number of grid points. The reconstruction of the corresponding velocity fields requires $O(N \log_2 N)$ operations owing to the use of FFTs. We have shown that these decompositions allow an efficient extraction of the coherent vortices out of turbulent flows. Indeed, the coherent vortices are represented by a few wavelet modes, that is 3%, and contain most, that is 99%, of the energy. The main differences between orthogonal and biorthogonal wavelet decompositions are that, for the latter, the incoherent flow is not structureless and the velocity PDF exhibits an exponential shape, while in the orthogonal case the incoherent flow is structureless and its velocity PDF is Gaussian. This may have some implications for modelling the effect of the incoherent background flow onto the coherent flow. In the biorthogonal case we found that neither enstrophy nor helicity are conserved (3.7% loss for both) owing to

the correlation between the coherent and incoherent vorticity, since this decomposition is not perfectly orthogonal. This is the main drawback of the biorthogonal decomposition.

In the orthogonal case, the threshold is known a priori, using theorems from denoising theory, and only depends on the number of grid points and on the total enstrophy of the flow. In the biorthogonal case, however, there is no way to a priori choose the threshold and this can only be done empirically. In the present paper we have chosen the threshold such that we retain the same number of wavelet coefficients for the coherent flow as for the orthogonal decomposition in order to compare their results for the same compression rate.

In future work we will implement the iterative algorithm proposed in [6], the convergence properties of which have been recently demonstrated in [14]. It automatically chooses the threshold value for the orthogonal decomposition, which no longer depends on the total enstrophy since the variance of the incoherent background vorticity is now estimated by an iterative procedure. We will also study the influence of orthogonal and biorthogonal wavelet filtering on the dynamics of flow to asses the properties of both decompositions for performing CVSs, which deterministically compute the evolution of the coherent flow in an adaptive wavelet basis, while statistically modelling the influence of the incoherent flow on the coherent flow or discarding it.

Acknowledgements

We would like to thank Giulio Pellegrino for providing us with the code of orthogonal wavelet decomposition and analysis, and Maurice Meneguzzi for providing us with the 3D dataset. This work has been partially supported by the French–German Programme DFG-CNRS ‘LES and CVS of complex flows’ and by the contract CEA-Euratom-ENS no. V.3258.001.

References

[1] Farge, M., 1992, Wavelet transforms and their applications to turbulence. *Annual Review of Fluid Mechanics*, **24**, 395–457.

[2] Farge, M., Pellegrino, G. and Schneider, K., 2001, Coherent vortex extraction in 3D turbulent flows using orthogonal wavelets. *Physical Review Letters*, **87**(5), 054501.

[3] Farge, M., Schneider, K., Pellegrino, G., Wray, A.A. and Rogallo, R.S., 2003, Coherent vortex extraction in three-dimensional homogeneous turbulence: comparision between CVS-wavelet and POD-Fourier decompositions. *Physics of Fluids*, **15**(10), 2886–2896.

[4] Schneider, K., Farge, M., Pellegrino, G. and Rogers, M., 2005, Coherent vortex simulation of three–dimensional turbulent mixing layers using orthogonal wavelets. *Journal of Fluid Mechanics*, **534**, 39–66.

[5] Farge, M. and Schneider, K., 2001, Coherent Vortex Simulation (CVS), a semi-deterministic turbulence model using wavelets. *Flow, Turbulence and Combustion*, **66**(4), 393–426.

[6] Farge, M., Schneider, K. and Kevlahan, N., 1999, Non-gaussianity and coherent vortex simulation for two-dimensional turbulence using an adaptive orthonormal wavelet basis. *Physics of Fluids*, **11**(8), 2187–2201.

[7] Donoho, D., 1993, Unconditional bases are optimal bases for data compression and statistical estimation. *Applied and Computational Harmonic Analysis*, **1**, 100–115.

[8] Donoho, D. and Johnstone, I., 1994, Ideal spatial adaptation via wavelet shrinkage. *Biometrika*, **81**, 425–455.

[9] Goldstein, D.E., Vasilyev, O.V., Wray, A.A. and Rogallo, R.S., 2000, Evaluation of the use of second generation wavelets in the coherent vortex simulation approach. In *Proceedings of Summer Programm*, Center for Turbulence Research, pp. 293–304.

[10] Goldstein, D.E. and Vasilyev, O.V., 2004, Stochastic coherent adaptive large eddy simulation method. *Physics of Fluids*, **16**(7), 2497–2512.

[11] Roussel, O., Schneider, K., Tsigulin, A. and Bockhorn, H., 2003, A conservative fully adaptive multiresolution algorithm for parabolic PDEs. *Journal of Computational Physics*, **188**(2), 493–523.

[12] Harten, A., 1995, Multiresolution algorithms for the numerical solution of hyperbolic conservation laws. *Communications of Pure and Applied Mathematics*, **48**, 1305–1342.

[13] Cohen, A., 2000, *Wavelet methods in numerical analysis*. In: P.G. Ciarlet and J.L. Lions (Eds). *Handbook of Numerical Analysis*, Vol. 7. Amsterdam: Elsevier.
[14] Azzalini, A., Farge, M. and Schneider, K., 2005, Nonlinear wavelet thresholding: A recursive method to determine the optimal denoising threshold. *Applied and Computational Harmonic Analysis*, **18**(2), 177–185.
[15] Vincent, A. and Meneguzzi, M., 1991, The spatial structure and statistical properties of homogeneous turbulence. *Journal of Fluid Mechanics*, **225**, 1–20.
[16] Moffatt, H.K., 1985, Magnetostatic equilibria and analogous Euler flows of arbitrarily complex topology. Part 1. Fundamentals. *Journal of Fluid Mechanics*, **159**, 359–478.